

Non-quantized Zak phases, PT/APT symmetry transitions, and doubly degenerate exceptional points in a non-Hermitian spin-orbit coupled SSH model

Jun-Xing Huo(霍俊行), Jian Li(李健), Qing-Xu Li(李清旭), and Jia-Ji Zhu(朱家骥)
Citation: Chin. Phys. B, 2025, 34 (**7**): 070301. DOI: 10.1088/1674-1056/adc7f3
Journal homepage: http://cpb.iphy.ac.cn; http://iopscience.iop.org/cpb

What follows is a list of articles you may be interested in

Ground state of SU(3) spin-orbit coupled soft-core Bose gas

Jia Liu(刘佳), Jing Feng(冯婧), Ya-Jun Wang(王雅君), Xiao-Fei Zhang(张晓斐), and Xue-Ying Yang(杨雪滢)
Chin. Phys. B, 2025, 34 (**6**): 060301. DOI: 10.1088/1674-1056/adc36b

Bessel vortices in spin-1 Bose-Einstein condensates with Zeeman splitting and spin-orbit coupling

Huan-Bo Luo(罗焕波), Xin-Feng Zhang(张鑫锋), Runhua Li(李润华), Yongyao Li(黎永耀), and Bin Liu(刘彬)
Chin. Phys. B, 2024, 33 (**10**): 100304. DOI: 10.1088/1674-1056/ad6424

Nonlinear modes coupling of trapped spin-orbit coupled spin-1 Bose-Einstein condensates

Jie Wang(王杰), Jun-Cheng Liang(梁俊成), Zi-Fa Yu(鱼自发), An-Qing Zhang(张安庆),Ai-Xia Zhang(张爱霞), and Ju-Kui Xue(薛具奎)
Chin. Phys. B, 2023, 32 (**9**): 090305. DOI: 10.1088/1674-1056/accd53

Electrical manipulation of a hole ‘spin’-orbit qubit in nanowire quantum dot: The nontrivial magnetic field effects

Rui Li(李睿) and Hang Zhang(张航)
Chin. Phys. B, 2023, 32 (**3**): 030308. DOI: 10.1088/1674-1056/ac873b

Spin-orbit coupling adjusting topological superfluid of mass-imbalanced Fermi gas

Jian Feng(冯鉴), Wei-Wei Zhang(张伟伟), Liang-Wei Lin(林良伟), Qi-Peng Cai(蔡启鹏), Yi-Cai Zhang(张义财), Sheng-Can Ma(马胜灿), and Chao-Fei Liu(刘超飞)
Chin. Phys. B, 2022, 31 (**9**): 090305. DOI: 10.1088/1674-1056/ac6860

Non-quantized Zak phases, PT/APT symmetry transitions, and doubly degenerate exceptional points in a non-Hermitian spin–orbit coupled SSH model

Jun-Xing Huo(霍俊行)[1], Jian Li(李健)[1,2,3,†], Qing-Xu Li(李清旭)[1,2,3], and Jia-Ji Zhu(朱家骥)[1,2,3,‡]

[1] *School of Science and Laboratory of Quantum Information Technology, Chongqing University of Posts and Telecommunications, Chongqing* 400065, *China*
[2] *Institute for Advanced Sciences, Chongqing University of Posts and Telecommunications, Chongqing* 400065, *China*
[3] *Southwest Center for Theoretical Physics, Chongqing University, Chongqing* 401331, *China*

(Received 13 February 2025; revised manuscript received 19 March 2025; accepted manuscript online 2 April 2025)

We theoretically investigate a one-dimensional Su–Schrieffer–Heeger (SSH) model with spin–orbit coupling (SOC) and sublattice-dependent gain and loss. As the gain and loss increase, the system transitions from a parity-time (PT) symmetric phase to a parity-time and anti-parity-time (PT&APT) symmetry-breaking phase, and finally to an anti-parity-time (APT) symmetric phase. Notably, when the intracell and intercell hopping, intracell and intercell SOC parameters are all equal to half the gain–loss parameter, the model exhibits a doubly degenerate exceptional point (EP). When the SOC is equal for intracell and intercell interactions, a stronger hopping mechanism within cells compared to that between cells results in an increase in SOC that transitions the Zak phase from zero to a non-quantized value, eventually arriving at one. In contrast, a reduction in the strength of intracell hopping leads the Zak phase to transition from two to a non-quantized value, eventually arriving at one. If the intracell and intercell SOC are not aligned, altering these couplings leads to a shift in the Zak phase from two to a non-quantized level, then to one, re-entering the non-quantized region, and eventually arriving at zero. We suggest a practical experimental setup for our model that can be implemented using electrical circuits.

Keywords: spin–orbit coupling, parity-time symmetry, Zak phase

PACS: 03.65.Yz, 71.70.Ej, 11.30.Er, 73.43.Nq

DOI: 10.1088/1674-1056/adc7f3 **CSTR:** 32038.14.CPB.adc7f3

1. Introduction

Spin–orbit coupling (SOC) is a relativistic phenomenon describing the interaction between an electron's spin and its orbital motion. In condensed matter physics, SOC significantly influences electron behavior, serving as a cornerstone in the understanding of both spin and topological phenomena. In spin physics, SOC leads to various phenomena, including the Dzyaloshinskii–Moriya (DM) interaction,[1–3] the spin Hall effect,[4,5] spin–orbit torque,[6–8] and skyrmions.[9,10] In topological physics, SOC can induce band structure inversion, facilitating transitions from topologically trivial to non-trivial states.[11,12] Additionally, SOC can lift band degeneracy, leading to the formation of degenerate nodal lines in certain energy bands, which give rise to Weyl semimetals.[13,14] The unique physical characteristics resulting from SOC have garnered significant interest among researchers. However, experimentally achieving precise control over spin and SOC in condensed matter systems remains challenging.[15,16] Consequently, there is a growing focus on simulating SOC-related spin and topological phenomena in classical systems, such as electrical circuits,[17–22] optical,[23–26] and acoustic systems,[27–29] which offer more manageable experimental conditions.

In the experimental simulation of condensed matter systems using classical analogs, the environments influence is often non-negligible. For instance, introducing gain and loss shifts the system from a Hermitian Hamiltonian to a non-Hermitian one. When the internal coupling balances these gains and losses, the system exhibits parity-time (PT) symmetry, resulting in a pseudo-Hermitian Hamiltonian that maintains real eigenvalues.[30–35] Once PT symmetry is broken, the energy spectrum transitions from real to complex conjugate pairs, and the point of transition — known as the exceptional point (EP) — is where eigenvalues and eigenstates coalesce.[36–42] This exceptional behavior near the EP makes PT-symmetric systems promising for quantum precision measurements,[43,44] quantum sensing,[45] and pre-threshold lasing applications.[46,47] Moreover, careful manipulation of the system's gain and loss can also reveal anti-parity-time (APT) symmetry.[48–50] This symmetry displays similar exceptional behavior to the corresponding EPs,[51] and shows potential in energy transfer and amplification.[52,53] Compared to PT symmetry, APT symmetry imposes less stringent conditions for dynamic balance, offering advantages for quantum computing and information processing applications.[54]

The Su–Schrieffer–Heeger (SSH) model is a widely stud-

†Corresponding author. E-mail: jianli@cqupt.edu.cn
‡Corresponding author. E-mail: zhujj@cqupt.edu.cn

© 2025 Chinese Physical Society and IOP Publishing Ltd. All rights, including for text and data mining, AI training, and similar technologies, are reserved.

ied theoretical framework for one-dimensional two-band lattice systems. It is often used to investigate topological phenomena and related effects in condensed matter physics.[55–58] A defining feature of the SSH model is its alternating hopping amplitudes between neighboring lattice sites. This chiral coupling strongly influences the system's topological characteristics.[59–63] By introducing gain and loss at specific lattice sites, one can observe phase transitions tied to both PT symmetry[64–67] and APT symmetry.[68–70] These gain and loss elements not only affect PT- and APT-symmetric phase transitions, but also impact topological phase transitions. For example, non-quantized Zak phases have been reported when PT symmetry is broken.[71] The incorporation of SOC into the non-Hermitian SSH model reveals additional rich phenomena. For instance, the interaction between non-reciprocal hopping and SOC can lead to both reciprocal and bipolar non-Hermitian skin effects.[72] Furthermore, spin-dependent gain and loss, when coupled with SOC, alter the PT symmetry of the system.[73] As gain and loss increase, the topological phase can degrade into a trivial phase. However, the complex interplay between sublattice-dependent gain and loss and SOC within the non-Hermitian SSH model remains an open avenue of exploration. Such studies could provide deeper insights into systems exhibiting both PT and APT symmetries.

This paper examines the combined effects of sublattice-dependent gain and loss and SOC on the system's properties. We find that increasing the gain and loss induces a transition from a PT-symmetric phase to a PT&APT symmetry-breaking phase, and eventually to an APT-symmetric phase. Notably, under the condition $v = w = \lambda = \gamma/2$, the system exhibits a doubly degenerate EP. When the SOC satisfies $\lambda = \lambda_v = \lambda_w$, if the intracell hopping exceeds the intercell hopping, increasing λ drives the Zak phase from $Z = 0$ into a non-quantized region and subsequently to $Z = 1$. Conversely, if the intracell hopping is smaller than the intercell hopping, the Zak phase transitions from $Z = 2$ into a non-quantized region and then to $Z = 1$ as λ increases. In contrast, when $\lambda_v \neq \lambda_w$, setting $\lambda_v = 1+\delta$ and $\lambda_w = 1-\delta$, increasing δ drives the Zak phase from $Z = 2$ to a non-quantized regime, then to $Z = 1$, subsequently re-entering the non-quantized regime, and finally transitioning to $Z = 0$. Finally, we map the Hamiltonian matrix of the model to the Laplacian matrix of an electrical circuit system, providing a new perspective for experimental simulation and theoretical analysis.

2. Model and method

This study introduces sublattice-dependent gain and loss combined with SOC to explore their interplay in the SSH model. The one-dimensional non-Hermitian SSH model with SOC is shown in Fig. 1, and the corresponding Hamiltonian is given by

$$\begin{aligned} H =& \sum_{i=1}^{N}\sum_{\sigma}(v c_{ia\sigma}^{\dagger} c_{ib\sigma} + \text{h.c.}) + \sum_{i=1}^{N-1}\sum_{\sigma}(w c_{ib\sigma}^{\dagger} c_{(i+1)a\sigma} + \text{h.c.}) \\ &+ \sum_{i=1}^{N}\sum_{\sigma\sigma'}(\lambda_v c_{ia\sigma}^{\dagger} c_{ib\sigma'} + \text{h.c.}) \\ &- \sum_{i=1}^{N-1}\sum_{\sigma\sigma'}(\lambda_w c_{ib\sigma}^{\dagger} c_{(i+1)a\sigma'} + \text{h.c.}) \\ &+ \sum_{i=1}\mathrm{i}\gamma(-c_{ia\sigma}^{\dagger} c_{ia\sigma} - c_{ia\sigma'}^{\dagger} c_{ia\sigma'} + c_{ib\sigma}^{\dagger} c_{ib\sigma} + c_{ib\sigma'}^{\dagger} c_{ib\sigma'}), \end{aligned} \tag{1}$$

where N denotes the number of unit cells. $c_{i\alpha\sigma}$ and $c_{i\alpha\sigma}^{\dagger}$ represent the annihilation and creation operators, respectively, for a particle with spin σ ($\sigma = \uparrow, \downarrow$) on sublattice α ($\alpha = a, b$) of the i-th unit cell. The intracell and intercell hoppings are denoted by v and w, respectively, while the intracell and intercell SOC hoppings are represented by λ_v and λ_w, respectively.

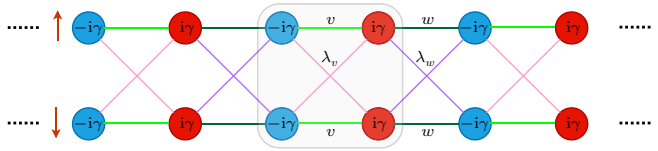


Fig. 1. A schematic diagram of the SOC SSH model with sublattice-dependent gain and loss. The two sublattices (a and b) are distinguished by blue and red colors, representing sublattices a and b, respectively. The imaginary potentials $-\mathrm{i}\gamma$ and $\mathrm{i}\gamma$ denote the gain and loss, respectively. Spin-up and spin-down states are indicated by upward and downward arrows. The light green and dark green solid lines represent the intracell hopping v and intercell hopping w, respectively. The magenta and purple solid lines correspond to the intracell-SOC hopping λ_v and the intercell-SOC hopping λ_w, respectively.

For this model under periodic boundary conditions (PBCs), we can add the term $H_{\text{PBC}} = \sum_{\sigma}(w c_{Nb\sigma}^{\dagger} c_{1a\sigma} + \text{h.c.}) - \sum_{\sigma\sigma'}(\lambda_w c_{Nb\sigma}^{\dagger} c_{1a\sigma'} + \text{h.c.})$ to Eq. (1). Applying the Fourier transform $c_{i\alpha\sigma} = \frac{1}{N}\sum_k c_{k\alpha\sigma}\mathrm{e}^{\mathrm{i}kn}$, we obtain the Hamiltonian in momentum space as

$$H = \begin{pmatrix} -\mathrm{i}\gamma & 0 & v + w\mathrm{e}^{-\mathrm{i}k} & \lambda_v - \lambda_w\mathrm{e}^{-\mathrm{i}k} \\ 0 & -\mathrm{i}\gamma & \lambda_v - \lambda_w\mathrm{e}^{-\mathrm{i}k} & v + w\mathrm{e}^{-\mathrm{i}k} \\ v + w\mathrm{e}^{\mathrm{i}k} & \lambda_v - \lambda_w\mathrm{e}^{\mathrm{i}k} & \mathrm{i}\gamma & 0 \\ \lambda_v - \lambda_w\mathrm{e}^{\mathrm{i}k} & v + w\mathrm{e}^{\mathrm{i}k} & 0 & \mathrm{i}\gamma \end{pmatrix}, \tag{2}$$

here, k is the Bloch wave vector. By diagonalizing the Hamiltonian, the energy band structure of the system is obtained as

$$\begin{aligned} E_{1,3} &= \pm\sqrt{(A_{\pm})^2 + (B_{\mp})^2 + 2(A_{\pm})(B_{\mp})\cos k - \gamma^2}, \\ E_{2,4} &= -E_{1,3}, \end{aligned} \tag{3}$$

where $A_{\pm} = (v \pm \lambda_v)$, $B_{\mp} = (w \mp \lambda_w)$, and the corresponding wave function is

$$\psi_{1,2} = \left(\frac{\mp\mathrm{e}^{-\frac{\mathrm{i}k}{2}}(\pm\mathrm{i}\gamma + E_{1,3})}{\mathrm{e}^{-\frac{\mathrm{i}k}{2}}A_{+} + \mathrm{e}^{\frac{\mathrm{i}k}{2}}B_{-}}, \frac{\mp\mathrm{e}^{-\frac{\mathrm{i}k}{2}}(\pm\mathrm{i}\gamma + E_{1,3})}{\mathrm{e}^{-\frac{\mathrm{i}k}{2}}A_{+} + \mathrm{e}^{\frac{\mathrm{i}k}{2}}B_{-}}, 1, 1 \right)^{\mathrm{T}},$$

$$\psi_{3,4}=\left(\frac{\pm e^{-\frac{ik}{2}}(\pm i\gamma+E_{2,4})}{e^{-\frac{ik}{2}}A_-+e^{\frac{ik}{2}}B_+},\frac{\mp e^{-\frac{ik}{2}}(\pm i\gamma+E_{2,4})}{e^{-\frac{ik}{2}}A_-+e^{\frac{ik}{2}}B_+},-1,1\right)^{\mathrm{T}}. \quad (4)$$

In this model, time-reversal symmetry (TRS) is defined as $T_+H^*(k)T_+^{-1}=H(-k)$, and particle–hole symmetry (PHS) is defined as $C_-H^{\mathrm{T}}(k)C_-^{-1}=-H(-k)$. The conjugate of TRS, denoted as TRS†, is given by $T_-H^*(k)T_-^{-1}=-H(-k)$, while the conjugate of PHS, denoted as PHS†, is defined as $C_+H^{\mathrm{T}}(k)C_+^{-1}=H(-k)$. In our model, both TRS† and PHS† symmetries are satisfied. The corresponding symmetry operators are $C_+=\sigma_0\otimes\sigma_0$ (with $C_+^2=1$), $T_-=\sigma_z\otimes\sigma_0$ (with $T_-T_-^*=1$). This classification places the system in the BDI† symmetry class, which supports a $\mathbb{Z}$-type topological invariant.[74] The corresponding Zak phase is defined as

$$Z=\frac{1}{2\pi}\sum_n i\oint\langle\varphi_n|\partial_k\psi_n\rangle, \quad (5)$$

where $|\psi_n\rangle$ and $\langle\varphi_n|$ represent the right and left eigenstates of the system, respectively. These eigenstates satisfy the relations $H_k|\psi_n\rangle=E_n|\psi_n\rangle$, $H_k^\dagger|\varphi_n\rangle=E_n^*|\varphi_n\rangle$, and $\langle\varphi_m|\psi_n\rangle=\delta_{mn}$.

To compute the Zak phase numerically, we employ the Wilson loop approach.[75] The momentum space in the first Brillouin zone, $-\pi\leqslant k<\pi$, is discretized into N segments, approximating the Berry connection integral as a summation over these segments. For each interval $[k_i,k_{i+1}]$ ($i=1,2,\ldots,N$, with $k_{N+1}=k_1$), the contribution θ_i is given by $e^{-i\theta_i}=\langle\varphi_{m,k_i}|\psi_{m,k_{i+1}}\rangle$, where $\langle\varphi_{m,k_i}|\psi_{m,k_{i+1}}\rangle$ represents the inner product between the left and right eigenstates of the m-th band at momentum points k_i and k_{i+1}. The overall integral is then computed as a product of these contributions. As shown in Eq. (3), due to the presence of two energy bands below the band gap, the Berry connection is represented as a matrix: $M_{ll'}^{k_i,k_{i+1}}=\langle\varphi_{l,k_i}|\psi_{l',k_{i+1}}\rangle$, $l,l'\in\{1,2\}$, where l and l' label the two bands. By multiplying the N matrices $M^{k_i,k_{i+1}}$, we obtain the Wilson loop matrix W. Finally, the Zak phase, which serves as a topological invariant, is determined from the eigenvalues w_l of W as $\mathrm{Zak}=\sum_{l=1,2}i\log(w_l)$.

3. PT and APT phase transitions

The non-Hermitian Hamiltonian in this study possesses a parity operator $P=(\sigma_x\otimes\sigma_x)$ and a time-reversal operator $T=(\sigma_0\otimes\sigma_x)\kappa$, where $\sigma_{x,y,z}$ are the Pauli matrices, σ_0 is the 2×2 identity matrix, and κ denotes the complex conjugation operator (representing the time-reversal operation). Because of $PTH(PT)^{-1}=H$, the non-Hermitian Hamiltonian possesses PT symmetry. For the corresponding wave functions, when Eq. (3) is entirely real, i.e., $\|v+\lambda_v|-|w-\lambda_w\|>\gamma$ and $\|v-\lambda_v|-|w+\lambda_w\|>\gamma$, the following holds: $PT\psi_{1,2}=\psi_{1,2}$ and $PT\psi_{3,4}=\psi_{3,4}$. At this point, the wave function simultaneously satisfies PT symmetry. However, when Eq. (3) becomes complex, i.e., when $\|v+\lambda_v|-|w-\lambda_w\|<\gamma$ or $\|v-\lambda_v|-|w+\lambda_w\|<\gamma$, the relations change to $PT\psi_{1,2}\neq\psi_{1,2}$ and $PT\psi_{3,4}\neq\psi_{3,4}$. In this case, the wave function no longer satisfies PT symmetry. On the other hand, the combination of chiral and time-reversal symmetries suggests another operator: APT symmetry,[69,76] expressed as $(\sigma_z\otimes\sigma_0)T$. Similar to PT symmetry, the Hamiltonian always satisfies the anticommutation relation with the APT operator: $(\mathrm{APT})H(\mathrm{APT})^{-1}=-H$. For the wave function, when all terms in Eq. (3) are purely imaginary, i.e., when $|v+\lambda_v|+|w-\lambda_w|<\gamma$ and $|v-\lambda_v|+|w+\lambda_w|<\gamma$, the following holds: $(\mathrm{APT})\psi_{1,2}=-\psi_{1,2}$ and $(\mathrm{APT})\psi_{3,4}=-\psi_{3,4}$. At this point, the system possesses APT symmetry. However, when Eq. (3) is not purely imaginary, that is, if either $|v+\lambda_v|+|w-\lambda_w|>\gamma$ or $|v-\lambda_v|+|w+\lambda_w|>\gamma$, the relations become $(\mathrm{APT})\psi_{1,2}\neq-\psi_{1,2}$ and $(\mathrm{APT})\psi_{3,4}\neq-\psi_{3,4}$. In this case, the system does not possess APT symmetry. If none of these conditions are satisfied, the system is in the PT&APT symmetry-broken phase.

Subsequently, we numerically analyze the combined effects of γ and λ on PT and APT symmetries. To simplify the analysis, let $\lambda=\lambda_v=\lambda_w$ and fix the parameters as $v=1$ and $w=0.5$ or 1.5. The corresponding phase diagrams are shown in Figs. 2(a) and 2(b). The system is clearly divided into three distinct regions, namely, the PT symmetric phase, the PT and APT symmetry-broken phase, and the APT symmetric phase, consistent with the previous analysis. When $\|v+\lambda_v|-|w-\lambda_w\|>\gamma$ and $\|v-\lambda_v|-|w+\lambda_w\|>\gamma$, the system resides in the PT symmetric phase, with the energy spectrum shown in (a1) and (b1). Under PBCs, the energy spectrum is entirely real, while under open boundary conditions (OBCs), edge states emerge, confirming the bulk–boundary correspondence. When neither $\|v+\lambda_v|-|w-\lambda_w\|>\gamma$ and $\|v-\lambda_v|-|w+\lambda_w\|>\gamma$ nor $|v+\lambda_v|+|w-\lambda_w|<\gamma$ and $|v-\lambda_v|+|w+\lambda_w|<\gamma$ are satisfied, the system enters the PT and APT symmetry-broken phase. In this phase, as shown in (a2) and (b2), the energy spectrum becomes complex under both PBCs and OBCs. When $|v+\lambda_v|+|w-\lambda_w|<\gamma$ and $|v-\lambda_v|+|w+\lambda_w|<\gamma$, the system transitions into the APT symmetric phase, where the energy spectrum is purely imaginary. Overall, when $\gamma=0$, the system remains in the PT symmetry-protected phase, with $\lambda=\frac{|v-w|}{2}$ marking the EP. For $0<\gamma<v+w$, the system transitions from the EP into the PT and APT symmetry-broken phase. When $\gamma>v+w$, the system further transitions into the APT symmetric phase. At this stage, regardless of variations in λ, the system cannot revert to the PT symmetry-protected phase. Based on the band structure expression (3), the condition for a doubly degenerate EP requires that, for all values of k, $E_1=E_2=0$ and $E_3=E_4=0$. This condition can be expressed as $(v\pm\lambda_v)^2+(w\mp\lambda_w)^2+2(v\pm\lambda_v)(w\mp\lambda_w)\cos k=0$ for all k. Specifically, by tuning the relevant parameters, the scenario depicted in Fig. 2(c) can be achieved, where point (c1) rep-

resents the doubly degenerate EP. For simplification, setting $w = \lambda$ or $v = \lambda$, the condition for the EP line can be reduced to $[(v+\lambda)^2 - \gamma^2] = 0$ and $[(w+\lambda)^2 - \gamma^2] = 0$. When both conditions are satisfied, the system reaches a doubly degenerate EP

$$v = w = \lambda = \gamma/2. \tag{6}$$

When the system parameters satisfy Eq. (6), the two EP lines intersect. At the intersection point of these two EP lines, all energy eigenvalues are zero, as shown in Fig. 2(c1). However, despite the zero energy eigenvalues, the corresponding wave functions belong to two distinct states, resulting in the degeneracy of the EP.

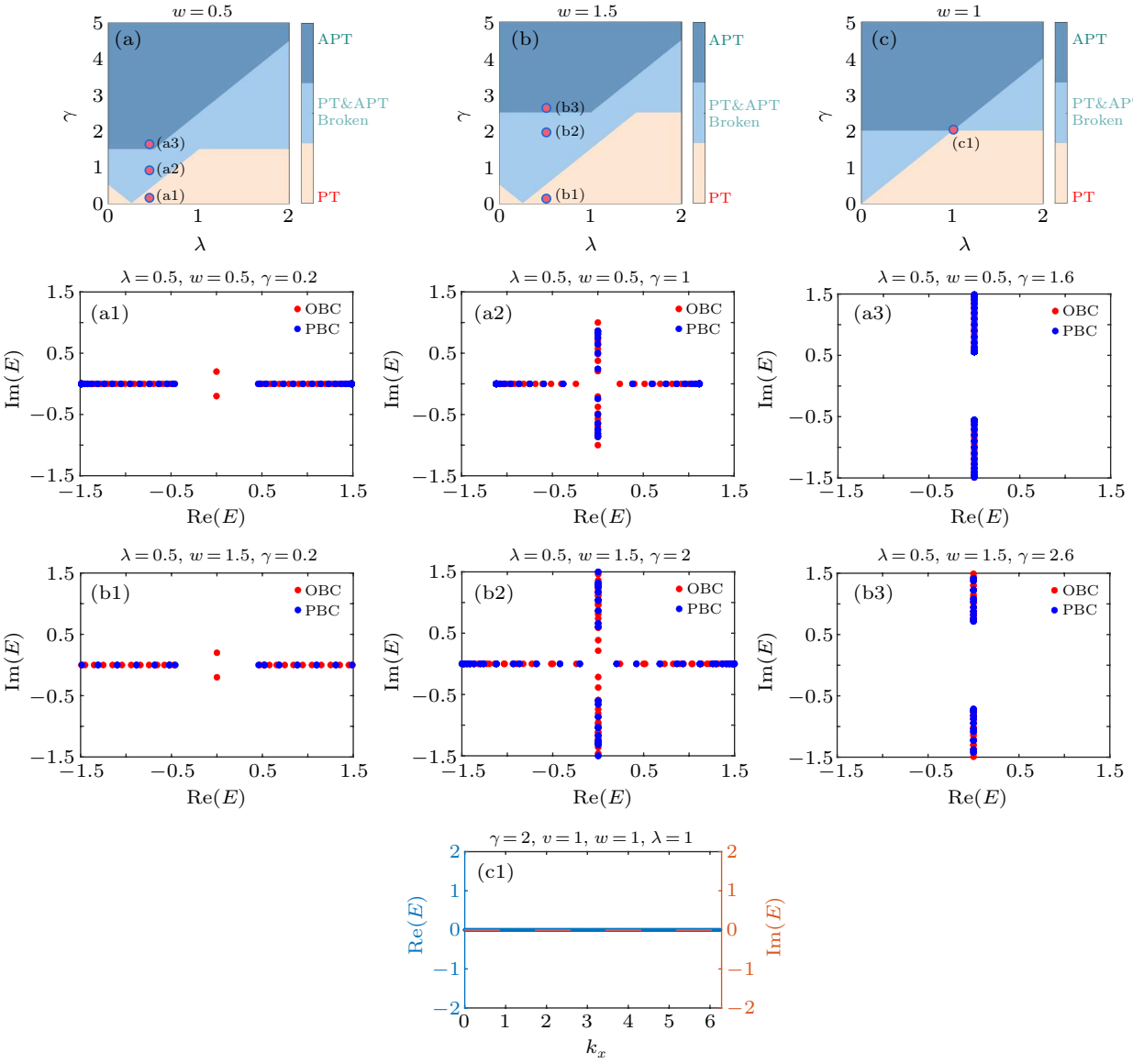


Fig. 2. Phase diagrams of PT and APT symmetries. (a), (b), and (c) correspond to the phase diagrams for intercell hopping w set to 0.5, 1.5, and 1, respectively. Here, γ represents the imaginary potential associated with gain and loss, and λ denotes the SOC. The three colored regions in the phase diagrams indicate the PT symmetric phase, the PT and APT symmetry-broken phase, and the APT symmetric phase, respectively. (a1)–(a3) and (b1)–(b3) display the band structures at specific points in phase diagrams (a) and (b), respectively, where the horizontal axis represents the real part of the energy, and the vertical axis represents the imaginary part. OBCs and PBCs are indicated by red and blue points, respectively. (c1) shows the band structure corresponding to the doubly degenerate EP in phase diagram (c), where the blue curve represents the real energy spectrum, and the red curve represents the imaginary energy spectrum. Other parameters are set to $v = 1$.

4. Topological phase

For the study of topological invariants, we fix $v = 1$ and choose $w = 0.5$ or $w = 1.5$, corresponding to the trivial and non-trivial phases of the conventional SSH model, respectively. To simplify the analysis, we first consider the case where $\lambda = \lambda_v = \lambda_w$.

From Fig. 3(a), when the intracell hopping exceeds the intercell hopping, if $\gamma < -2\lambda + |v - w|$, the system is in the $Z = 0$ region. The energy spectrum and probability density are shown in Figs. 3(a1) and 3(a1-density), respectively. Under PBCs, the energy spectrum is entirely real; under OBCs, there are no edge states, indicating that the

system is in the PT symmetric phase and is topologically trivial. If $-2\lambda + |v-w| < \gamma < 2\lambda - |v-w|$, the system enters a non-quantized region where the Zak phase is not well-defined. Within this region, the topological invariants can take values of $Z = 1$ (or 0) under certain parameter variations. Under PBCs, the energy spectrum becomes complex, as shown in Figs. 3(a2) and 3(a2′); the corresponding probability densities reveal the presence of nearly one pair of edge states [see Fig. 3(a2′-density)] or their absence [see Fig. 3(a2-density)], depending on the parameters. If $\gamma > 2\lambda - |v-w|$, the system transitions to the $Z = 1$ region. The energy spectrum and probability density are shown in Figs. 3(a3) and 3(a3-density), respectively. Under PBCs, the energy spectrum is entirely real; under OBCs, a set of edge states emerges, indicating that the system is in the PT symmetric phase and is topologically non-trivial. As shown in Fig. 3(b), when the intracell hopping is smaller than the intercell hopping, if $\gamma < -2\lambda + |v-w|$, the system is in the

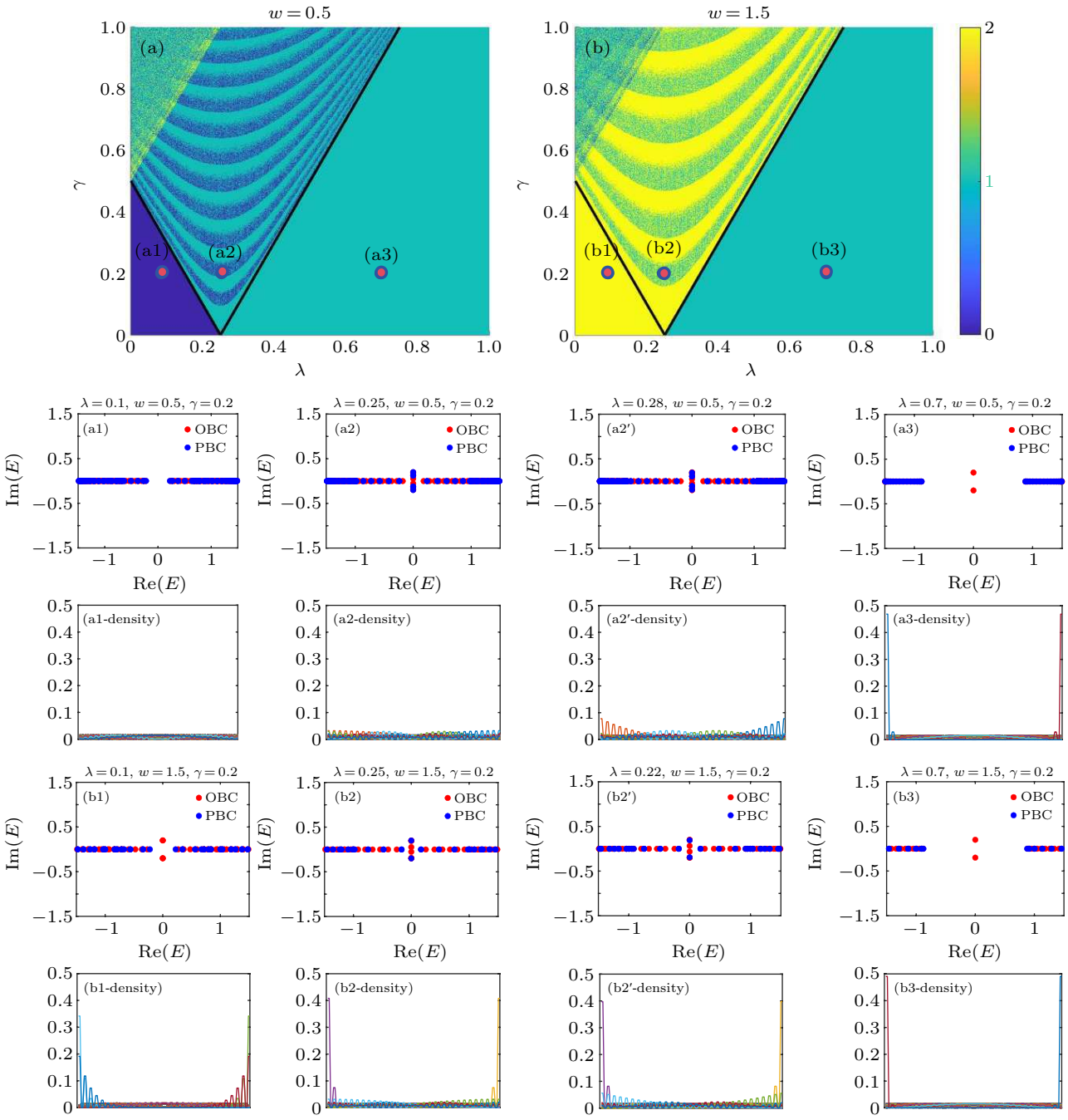


Fig. 3. Zak phase diagrams varying with γ and λ. (a) and (b) correspond to the Zak phase diagrams for intercell coupling $w = 0.5$ and $w = 1.5$, respectively. The blue region represents the topologically trivial phase with topological invariant $Z = 0$, the green and yellow regions represent the topologically non-trivial phases with topological invariants $Z = 1$ and $Z = 2$, respectively. (a1)–(a3) and (b1)–(b3) correspond to the energy at specific points in diagrams (a) and (b), where the red and blue dots represent OBCs and PBCs, respectively. (a1-density)–(a3-density) and (b1-density)–(b3-density) show the corresponding probability density distributions. The specific parameters are as follows: (a1) $\gamma = 0.2$, $\lambda = 0.1$, $w = 0.5$; (a2) $\gamma = 0.2$, $\lambda = 0.25$, $w = 0.5$; (a2′) $\gamma = 0.2$, $\lambda = 0.28$, $w = 0.5$; (a3) $\gamma = 0.2$, $\lambda = 0.7$, $w = 0.5$; (b1) $\gamma = 0.2$, $\lambda = 0.1$, $w = 1.5$; (b2) $\gamma = 0.2$, $\lambda = 0.25$, $w = 1.5$; (b2′) $\gamma = 0.2$, $\lambda = 0.22$, $w = 1.5$; (b3) $\gamma = 0.2$, $\lambda = 0.7$, $w = 1.5$. The other parameter is $v = 1$.

$Z = 2$ region. The energy spectrum and probability density are shown in Figs. 3(b1) and 3(b1-density), respectively. Under PBCs, the energy spectrum is entirely real; under OBCs, two sets of edge states appear, and the system is in the PT symmetric phase and is topologically non-trivial. If $-2\lambda + |v - w| < \gamma < 2\lambda - |v - w|$, the system enters a non-quantized region where the Zak phase is not well-defined. Within this region, the topological invariants can take values of $Z = 1$ (or 2) under certain parameter variations. Under PBCs, the energy spectrum becomes complex, as shown in Figs. 3(b2) and 3(b2′); the corresponding probability densities show the presence of one pair of edge states [see Fig. 3(b2′-density)] or nearly two pairs of edge states [see Fig. 3(b2-density)], depending on the parameters. If $\gamma > 2\lambda - |v - w|$, the system transitions to the $Z = 1$ region. The energy spectrum and probability density are shown in Figs. 3(b3) and 3(b3-density), respectively. Under PBCs, the energy spectrum is entirely real; under OBCs, a set of edge states emerges, indicating that the system is in the PT symmetric phase and is topologically non-trivial. Comparative analysis reveals that variations in γ drive the system into the non-quantized region $-2\lambda + |v - w| < \gamma < 2\lambda - |v - w|$, where the Zak phase becomes invalid.[71] This occurs because the system enters the PT symmetry-broken phase, and the real part of the complex Berry phase is no longer strictly quantized under PT symmetry protection. As λ increases, the topological number (Zak phase) transitions from $Z = 0$ or $Z = 2$ into the non-quantized region and then changes to $Z = 1$.

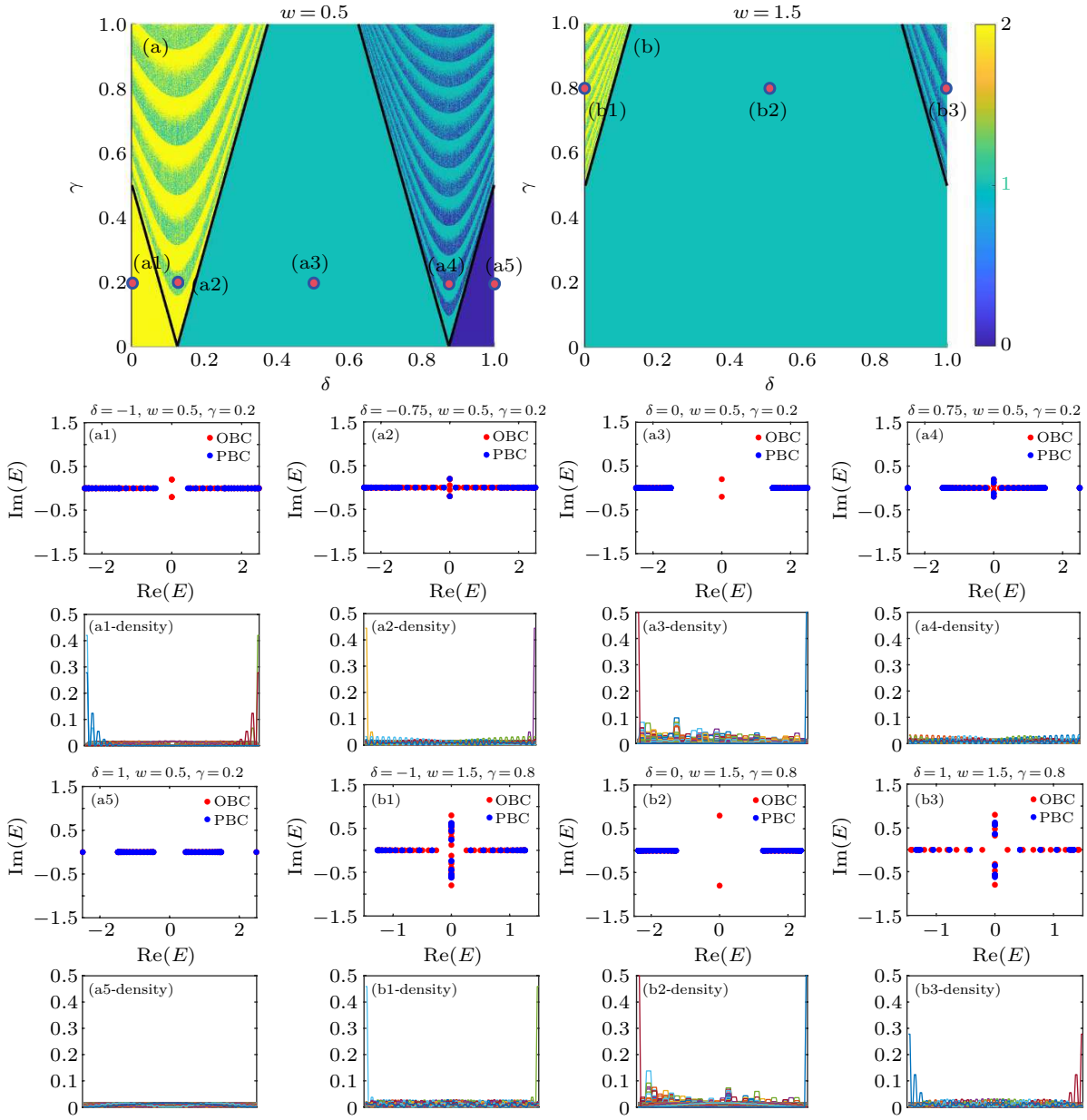


Fig. 4. Zak phase diagrams varying with δ and γ. (a) and (b) represent the Zak phase diagrams for intercell coupling $w = 0.5$ and $w = 1.5$, respectively. (a1)–(a5) and (b1)–(b3) show the energy band diagrams at selected points in the phase diagrams (a) and (b), OBCs and PBCs are represented by red and blue points, respectively. (a1-density)–(a5-density) and (b1-density)–(b3-density) show the corresponding probability density distributions. Specifically, in (a), the parameters are $\gamma = 0.2$ with $\delta = -1$, -0.75, 0, 0.75, and 1, and $w = 0.5$. In (b), the parameters are $\gamma = 0.8$ with $\delta = -1$, 0, and 1, and $w = 1.5$. The other parameter is set as $v = 1$.

For the case of $\lambda_v \neq \lambda_w$, we set the intracell-SOC is $\lambda_v = (1+\delta)$, and the intercell-SOC is $\lambda_w = (1-\delta)$. According to the analysis in Fig. 4(a), when the intracell hopping exceeds the intercell hopping, the behavior of the energy spectrum and probability density depends on the value of γ. Specifically, when $\gamma < -2\delta - |v+w|$, the system is in the $Z = 2$ region. Under PBCs, the energy spectrum is entirely real, and under OBCs, two sets of edge states appear, indicating that the system is in the PT symmetric phase and is topologically non-trivial, as shown in Figs. 4(a1) and 4(a1-density). When $-2\delta - |v+w| < \gamma < 2\delta + |v+w|$, the system is in the non-quantized region. The energy spectrum under PBCs is complex, and one set of edge states appears under OBCs, placing the system in the PT symmetry-broken phase, as shown in Figs. 4(a2) and 4(a2-density). When $2\delta + |v+w| < \gamma < -2\delta + |v+w|$, the system is in the $Z = 1$ region. The energy spectrum under PBCs is entirely real, and one set of edge states appears under OBCs, indicating that the system is in the PT symmetric phase and is topologically non-trivial, as shown in Figs. 4(a3) and 4(a3-density). When $-2\delta + |v+w| < \gamma < 2\delta - |v+w|$, the system once again enters the non-quantized region. The PBC energy spectrum is complex, and no edge states appear under OBCs, placing the system in the PT symmetry-broken phase, as shown in Figs. 4(a4) and 4(a4-density). When $\gamma > 2\delta - |v+w|$, the system is in the $Z = 0$ region. The PBC energy spectrum is entirely real, and no edge states appear under OBCs, indicating that the system is in the PT symmetric phase and is topologically trivial, as shown in Figs. 4(a5) and 4(a5-density).

When the intracell hopping is less than the intercell hopping, as shown in Fig. 4(b), when $\gamma < 2\delta + |v+w|$, the system is in the non-quantized region. The PBC energy spectrum is complex, and one set of edge states appears under OBCs, placing the system in the PT symmetry-broken phase, as shown in Figs. 4(b1) and 4(b1-density). When $2\delta + |v+w| < \gamma < -2\delta + |v+w|$, the system is in the $Z = 1$ region. The PBC energy spectrum is entirely real, and one set of edge states appears under OBCs, indicating that the system is in the PT symmetric phase and is topologically non-trivial, as shown in Figs. 4(b2) and 4(b2-density). When $\gamma > -2\delta + |v+w|$, the system re-enters the non-quantized region. The PBC energy spectrum is complex, and one set of edge states appears under OBCs, placing the system in the PT symmetry-broken phase, as shown in Figs. 4(b3) and 4(b3-density).

By comparison, it is found that γ drives the system into the non-quantized regions within $-2\delta - |v+w| < \gamma < 2\delta + |v+w|$ and $-2\delta + |v+w| < \gamma < 2\delta - |v+w|$, where the Zak phase becomes invalid. This is because the system enters the PT symmetry-broken phase, and the real part of the complex Berry phase is no longer strictly quantized under PT symmetry protection. As δ increases, the topological invariant transitions from $Z = 2$ to the non-quantized region, then to $Z = 1$, re-enters the non-quantized region, and finally approaches $Z = 0$.

5. Circuit simulation experiment scheme

The SSH model with SOC and sublattice-dependent gain and loss can be simulated using a classical circuit model, as shown in Fig. 5. Each lattice site is represented by an *LC* resonant circuit, where gain and loss are simulated by resistors R and negative resistors, respectively. The hopping v and w, as well as the SOC hopping λ_v and λ_w, are represented by capacitors. To connect the circuit model with the system's Hamiltonian, the following steps are taken. First, the admittance of each component is determined. The admittance of a capacitor is $\mathrm{j}\omega C$, the admittance of an inductor is $1/(\mathrm{j}\omega L)$, and the admittance of a resistor is $1/R$. Considering PBCs, a unit cell is defined to contain four lattice sites in the order shown within the box in Fig. 5. Next, by applying Kirchhoff's current law, equations for the four lattice sites are derived to describe the relationship between the current and voltage at each site in the circuit:

$$\begin{aligned} I_i = & \frac{0-v_{i,n}}{\mathrm{j}\omega L} + \mathrm{j}\omega\Big[C_0(0-v_{i,n}) + C_w(v_{i+2,n-i} - v_{i,n}) \\ & + C_v(v_{i+2,n} - v_{i,n}) + C_{\lambda v}(v_{i+3,n} - v_{i,n}) \\ & + C_{\lambda w}(v_{i+3,n-1} - v_{i,n}) + \frac{0-v_{i,n}}{\omega R}\Big], \end{aligned} \tag{7}$$

where $i = 1,2,3,4$ represents the four lattice sites within the n-th unit cell. L denotes the inductor, R represents the resistor, and C_0, C_v, C_w, C_{λ_v}, and C_{λ_w} are capacitors with different values. The voltage at the i-th site in the n-th unit cell is denoted by $v_{i,n}$, and ω is the angular frequency of the alternating current. Based on the relationship between current, admittance, and voltage ($\boldsymbol{I}(\omega) = \boldsymbol{J}(\omega)\boldsymbol{V}(\omega)$), we can connect this to Eq. (7) and obtain the Laplacian matrix $\boldsymbol{J}(\omega)$, which corresponds to the Hamiltonian of the system,

$$\boldsymbol{J}(\omega) = \begin{pmatrix} \mu - \mathrm{j}\omega R & 0 & C_v + C_w\mathrm{e}^{-\mathrm{i}k} & C_{\lambda_v} - C_{\lambda_w}\mathrm{e}^{-\mathrm{i}k} \\ 0 & \mu - \mathrm{j}\omega R & C_{\lambda_v} - C_{\lambda_w}\mathrm{e}^{-\mathrm{i}k} & C_v + C_w\mathrm{e}^{-\mathrm{i}k} \\ C_v + C_w\mathrm{e}^{\mathrm{i}k} & C_{\lambda_v} - C_{\lambda_w}\mathrm{e}^{\mathrm{i}k} & \mu + \mathrm{j}\omega R & 0 \\ C_{\lambda_v} - C_{\lambda_w}\mathrm{e}^{\mathrm{i}k} & C_v + C_w\mathrm{e}^{\mathrm{i}k} & 0 & \mu + \mathrm{j}\omega R \end{pmatrix}, \tag{8}$$

where $\mu = \frac{1}{\omega^2 L} - C_0 - C_v - C_w - C_{\lambda_v} - C_{\lambda_w}$ reflects the influence of the inductor and capacitor configuration on the system's potential energy in the circuit. When the values of the inductors and capacitors are chosen such that $\mu = 0$, there is a one-to-one correspondence between the Laplacian matrix in Eq. (8) and the Hamiltonian in Eq. (2). However, even if it is not possible to set $\mu = 0$ by selecting specific values for the inductors and capacitors, the system's Hamiltonian will include a constant potential term. In this case, while the connection between the circuit system and the Hamiltonian remains valid, an additional fixed potential term must be introduced to fully describe the system's behavior.

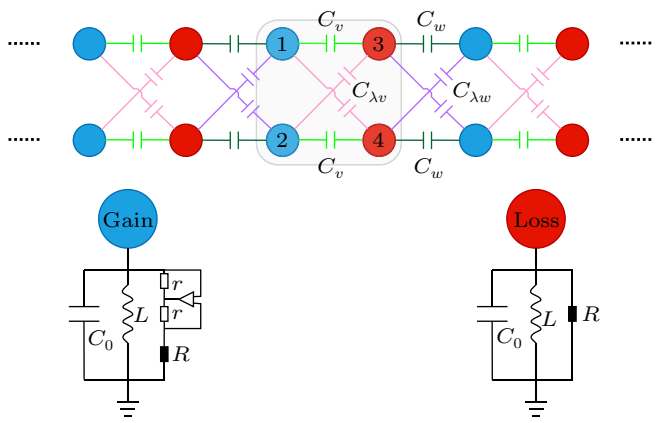


Fig. 5. Circuit schematic of the system. Blue indicates lattice sites with gain, while red indicates lattice sites with loss. The intracell hopping and intercell hopping are represented by capacitors C_v and C_w, respectively. The intracell-SOC and intercell-SOC are represented by capacitors C_{λ_v} and C_{λ_w}, respectively. Gain and loss are realized through resistors R and negative resistors, with the negative resistance implemented using an integrated negative impedance converter (INIC).

6. Conclusion

This work investigates the SSH model incorporating SOC and sublattice-dependent gain and loss. By analyzing the symmetries of the Hamiltonian and the wave functions, the conditions necessary for PT and APT symmetries are established. Numerical calculations are performed to produce phase diagrams characterizing these symmetries. When the condition $v = w = \lambda = \gamma/2$ is satisfied, the system exhibits a doubly degenerate EP. In addition, the Zak phase is calculated for cases where $\lambda = \lambda_v = \lambda_w$ and where $\lambda_v \neq \lambda_w$. We observe that the parameter γ induces non-quantized regions in which the Zak phase loses its quantization. Specifically, for $\lambda = \lambda_v = \lambda_w$, as λ increases, the topological invariant transitions from $Z = 0$ and $Z = 2$ into a non-quantized region and ultimately to $Z = 1$. For $\lambda_v \neq \lambda_w$, increasing δ causes the Zak phase to transition from $Z = 2$ into a non-quantized region, then to $Z = 1$, re-enter a non-quantized region, and finally settle at $Z = 0$. Finally, this study explores the simulation of the model in an electrical circuit framework and derives the corresponding Laplacian matrix, offering a practical approach for experimental realization and theoretical analysis.

Acknowledgments

Project supported by the Natural Science Foundation of Chongqing, China (Grant No. CSTB2024NSCQ-MSX0736), Science and Technology Innovation Key R&D Program of Chongqing (Grant No. CSTB2024TIAD-STX0035), and the Research Foundation of Institute for Advanced Sciences of CQUPT (Grant No. E011A2022328).

References

[1] Yang J H, Li Z L, Lu X Z, Whangbo M H, Wei S H, Gong X G and Xiang H J 2012 *Phys. Rev. Lett.* **109** 107203
[2] Qaiumzadeh A, Ado I A, Duine R A, Titov M and Brataas A 2018 *Phys. Rev. Lett.* **120** 197202
[3] Yang J, Li J, Lin L and Zhu J J 2020 *Chin. Phys. Lett.* **37** 087501
[4] Sinova J, Valenzuela S O, Wunderlich J, Back C H and Jungwirth T 2015 *Rev. Mod. Phys.* **87** 1213
[5] Yang W, Chang K and Zhang S C 2008 *Phys. Rev. Lett.* **100** 056602
[6] Manchon A and Zhang S 2009 *Phys. Rev. B* **79** 094422
[7] Zhou P, Wang Z, Liu J and Yu Z 2025 *Phys. Rev. B* **111** 035403
[8] Medina Duenas J, García J H and Roche S 2024 *Phys. Rev. Lett.* **132** 266301
[9] Banerjee S, Rowland J, Erten O and Randeria M 2014 *Phys. Rev. X* **4** 031045
[10] Rowland J, Banerjee S and Randeria M 2016 *Phys. Rev. B* **93** 020404
[11] Hu Y, Le C, Zhang Y, Zhao Z, Liu J, Ma J, Plumb N C, Radovic M, Chen H, Schnyder A P, *et al.* 2023 *Nat. Phys.* **19** 1827
[12] Hasan M Z and Kane C L 2010 *Rev. Mod. Phys.* **82** 3045
[13] Liu D, Liu E, Xu Q, Shen J, Li Y, Pei D, Liang A, Dudin P, Kim T, Cacho C, *et al.* 2022 *npj Quantum Mater.* **7** 11
[14] Bodo F, Desmarais J K and Erba A 2022 *Phys. Rev. B* **105** 125108
[15] de Leon N P, Itoh K M, Kim D, Mehta K K, Northup T E, Paik H, Palmer B S, Samarth N, Sangtawesin S and Steuerman D W 2021 *Science* **372** eabb2823
[16] Zhou X, Shen Q, Wang Y, Dai Y, Chen Y and Wu K 2024 *Natl. Sci. Rev.* **11** nwae272
[17] Wang Z, Zeng X T, Biao Y, Yan Z and Yu R 2023 *Phys. Rev. Lett.* **130** 057201
[18] Yang H, Song L, Cao Y and Yan P 2023 *Commun. Phys.* **6** 211
[19] Wu M, Zhao Q, Kang L, Weng M, Chi Z, Peng R, Liu J, Werner D H, Meng Y and Zhou J 2023 *Phys. Rev. B* **107** 064307
[20] Li Y, Zhang J H, Mei F, Xie B, Lu M H, Ma J, Xiao L and Jia S 2023 *Phys. Rev. Appl.* **20** 064042
[21] Yuan H, Zhang W, Zhou Z, Wang W, Pan N, Feng Y, Sun H and Zhang X 2023 *Adv. Sci.* **10** 2301128
[22] Rafi Ul Islam S, Siu Z B, Sahin H, Lee C H and Jalil M B 2022 *Phys. Rev. Res.* **4** 043108
[23] Yan Q, Hu X, Fu Y, Lu C, Fan C, Liu Q, Feng X, Sun Q and Gong Q 2021 *Adv. Opt. Mater.* **9** 2001739
[24] Vaidya S, Noh J, Cerjan A, Jörg C, Von Freymann G and Rechtsman M C 2020 *Phys. Rev. Lett.* **125** 253902
[25] Wang D, Yang B, Guo Q, Zhang R Y, Xia L, Su X, Chen W J, Han J, Zhang S and Chan C T 2021 *Light Sci. Appl.* **10** 83
[26] Parto M, Liu Y G, Bahari B, Khajavikhan M and Christodoulides D N 2020 *Nanophotonics* **10** 403
[27] Zhang Z, Hu B, Liu F, Cheng Y, Liu X and Christensen J 2020 *Phys. Rev. B* **101** 220102
[28] Zhang X, Zangeneh Nejad F, Chen Z G, Lu M H and Christensen J 2023 *Nature* **618** 687
[29] Geng Z G, Peng Y G, Lv H, Xiong Z, Chen Z and Zhu X F 2021 *J. Phys.: Condens. Matter* **34** 104001
[30] Jiang W C, Wu H, Li Q X, Li J and Zhu J J 2024 *Phys. Rev. B* **110** 155144
[31] Yi Y and Yang Z 2020 *Phys. Rev. Lett.* **125** 186802
[32] Bender C M and Boettcher S 1998 *Phys. Rev. Lett.* **80** 5243
[33] Bender C M 2007 *Rep. Prog. Phys.* **70** 947
[34] Guo C X, Wang X R, Wang C and Kou S P 2020 *Phys. Rev. B* **101** 144439
[35] Lei Z, Lee C H and Li L 2024 *Commun. Phys.* **7** 100

[36] Heiss W 2004 *J. Phys. A: Math. Gen.* **37** 2455
[37] Ding K, Fang C and Ma G 2022 *Nat. Rev. Phys.* **4** 745
[38] Deng Z L, Li F J, Li H, Li X and Alu A 2022 *Laser Photon. Rev.* **16** 2100617
[39] Xiao L, Deng T, Wang K, Wang Z, Yi W and Xue P 2021 *Phys. Rev. Lett.* **126** 230402
[40] Xiao L, Wang K, Zhan X, Bian Z, Kawabata K, Ueda M, Yi W and Xue P 2019 *Phys. Rev. Lett.* **123** 230401
[41] Yang Z, Schnyder A P, Hu J and Chiu C K 2021 *Phys. Rev. Lett.* **126** 086401
[42] Zhang S M, He T Y and Jin L 2024 *Chin. Phys. Lett.* **41** 027201
[43] Duggan R, Mann S A and Alu A 2022 *ACS Photonics* **9** 1554
[44] Wang Z, Liang Z, Hu J, Zhou P, Liu L, Hu G, Wang W and Ye M 2025 *Adv. Phys.* **8** 2400349
[45] Zhang M, Sweeney W, Hsu C W, Yang L, Stone A and Jiang L 2019 *Phys. Rev. Lett.* **123** 180501
[46] Li A, Wei H, Cotrufo M, Chen W, Mann S, Ni X, Xu B, Chen J, Wang J, Fan S, *et al.* 2023 *Nat. Nanotechnol.* **18** 706
[47] Zyablovsky A A, Doronin I V, Andrianov E S, Pukhov A A, Lozovik Y E, Vinogradov A P and Lisyansky A A 2021 *Laser Photon. Rev.* **15** 2000450
[48] Li Y, Peng Y G, Han L, Miri M A, Li W, Xiao M, Zhu X F, Zhao J, Al A, Fan S and Qiu C W 2019 *Science* **364** 170
[49] Konotop V V and Zezyulin D A 2018 *Phys. Rev. Lett.* **120** 123902
[50] Choi Y, Hahn C, Yoon J W and Song S H 2018 *Nat. Commun.* **9** 2182
[51] Jian Y, Wang Y, Guo Z, Hu S, Wu B, Yang Y and Chen H 2023 *Appl. Phys. Lett.* **123** 141702
[52] Nair J M, Mukhopadhyay D and Agarwal G 2021 *Phys. Rev. Lett.* **126** 180401
[53] Guo Z, Yang F, Zhang H, Wu X, Wu Q, Zhu K, Jiang J, Jiang H, Yang Y, Li Y, *et al.* 2024 *Natl. Sci. Rev.* **11** nwad172
[54] Fang Y L, Zhao J L, Chen D X, Zhou Y H, Zhang Y, Wu Q C, Yang C P and Nori F 2022 *Phys. Rev. Res.* **4** 033022
[55] Jin L and Song Z 2019 *Phys. Rev. B* **99** 081103
[56] Wu H and An J H 2020 *Phys. Rev. B* **102** 041119
[57] Wu H, Wang B Q and An J H 2021 *Phys. Rev. B* **103** L041115
[58] Li J R, Zhang L L, Cui W B and Gong W J 2022 *Phys. Rev. Res.* **4** 023009
[59] Wang Y, Wu H, McCandless G T, Chan J Y and Ali M N 2023 *Nat. Rev. Phys.* **5** 635
[60] Zhao X, Wang Z, Chen J and Wang B 2022 *Results Phys.* **35** 105360
[61] Zeng X L, Lai W X, Wei Y W and Ma Y Q 2024 *Chin. Phys. B* **33** 030310
[62] Li G Q, Wang B H, Tang J Y, Peng P and Dong L W 2023 *Chin. Phys. B* **32** 077102
[63] Bao X X, Guo G F and Tan L 2023 *Chin. Phys. B* **32** 020301
[64] Xiao L, Zhan X, Bian Z, Wang K, Zhang X, Wang X, Li J, Mochizuki K, Kim D, Kawakami N, *et al.* 2017 *Nat. Phys.* **13** 1117
[65] Liu S, Ma S, Yang C, Zhang L, Gao W, Xiang Y J, Cui T J and Zhang S 2020 *Phys. Rev. Appl.* **13** 014047
[66] Stegmaier A, Imhof S, Helbig T, Hofmann T, Lee C H, Kremer M, Fritzsche A, Feichtner T, Klembt S, Höfling S, *et al.* 2021 *Phys. Rev. Lett.* **126** 215302
[67] Cheng X T, Wang L F, Li Y Z, Hou D B, Yu J W, Li C H, Lin X, Liu F, Gao F and Jin C Y 2024 *Laser Photon. Rev.* **18** 2400218
[68] Wu H C, Jin L and Song Z 2021 *Phys. Rev. B* **103** 235110
[69] Hu B, Zhang Z, Yue Z, Liao D, Liu Y, Zhang H, Cheng Y, Liu X and Christensen J 2023 *Phys. Rev. Lett.* **131** 066601
[70] Wu H C, Yang X M, Jin L and Song Z 2020 *Phys. Rev. B* **102** 161101
[71] Dangel F, Wagner M, Cartarius H, Main J and Wunner G 2018 *Phys. Rev. A* **98** 013628
[72] Jiang W C, Li J, Li Q X and Zhu J J 2023 *Appl. Phys. Lett.* **123** 201107
[73] Li J R, Wang Z A, Xu T T, Zhang L L and Gong W J 2023 *Prog. Theor. Exp. Phys.* **2023** 023
[74] Kawabata K, Shiozaki K, Ueda M and Sato M 2019 *Phys. Rev. X* **9** 041015
[75] Wang H X, Guo G Y and Jiang J H 2019 *New J. Phys.* **21** 093029
[76] Longhi S 2018 *Opt. Lett.* **43** 4025